

Magnetic field amplification in proto-neutron stars the role of the neutron-finger instability for dynamo excitation

L. Naso¹, L. Rezzolla^{2,3,4}, A. Bonanno⁵, and L. Paternò⁶

¹ SISSA - International School for Advanced Studies, Via Beirut 2-4, I-34014 Trieste, Italy

² Max-Planck Institut für Gravitationsphysik, Albert Einstein Institut, Am Mühlenberg 1, D-14476 Golm, Germany

³ Department of Physics and Astronomy, Louisiana State University, 202 Nicholson Hall, Tower Dr., Baton Rouge, LA 70803, USA

⁴ INFN, Sezione di Trieste, Via A. Valerio 2, I-34127 Trieste, Italy

⁵ INAF – Astrophysical Observatory of Catania, Via S. Sofia 78, I-95123 Catania, Italy

⁶ Department of Physics and Astronomy, Astrophysics Section, University of Catania, Via S. Sofia 78, I-95123 Catania, Italy

Received; accepted

ABSTRACT

Aims. During the first 40 s after their birth, proto-neutron stars are expected to be subject to at least two types of instability. The first one, the *convective* instability, is excited in the inner regions, where the entropy gradient produces a Rayleigh-type convection. The second one, the *neutron-finger* instability, is instead excited in the outer layers where the lepton gradients are large. Both instabilities involve convective motions and hence can trigger dynamo actions that may be responsible for the large magnetic fields in neutron stars and magnetars. However, because they have rather different mean turbulent velocities, they are also likely to give rise to different types of dynamo.

Methods. We have solved the mean-field induction equation in a simplified one-dimensional model of both the convective and the neutron-finger instability zones. Although very idealized, the model includes the nonlinearities introduced by the feedback processes that tend to saturate the growth of the magnetic field (α -quenching) and suppress its turbulent diffusion (η -quenching). The possibility of a dynamo action is studied within a dynamical model of turbulent diffusivity where the boundary of the unstable zone is allowed to move. A large number of numerical simulations have been performed in which the relevant parameters, such as the spin-period, the strength of the differential rotation, the intensity of the initial magnetic field, and the extent of the neutron finger instability zone, have been suitably varied.

Results. We show that the dynamo action can also be operative within a dynamical model of turbulent diffusivity and that the amplification of the magnetic field can still be very effective. Furthermore, we confirm the existence of a critical spin-period, below which the dynamo is always excited independently of the degree of differential rotation, and whose value is related to the size of the neutron-finger instability zone. We provide a relation for the intensity of the final field as a function of the spin of the star and of its differential rotation.

Conclusions. Although they were obtained by using a toy model, we expect that our results are able to capture the qualitative and asymptotic behaviour of a mean-field dynamo action developing in the neutron-finger instability zone. Overall, we find that such a dynamo is very efficient in producing magnetic fields well above equipartition, and thus that it could represent a possible explanation for the large surface magnetic fields observed in neutron stars.

Key words. Magnetohydrodynamics (MHD) – stars: neutron – turbulence – instabilities – stars: magnetic fields – stars: rotation

1. Introduction

The present understanding of the processes that produce the large magnetic field strengths observed in neutron stars (NSs) is still far from being complete. Most of the information about their magnetic fields is in fact derived either from their X-ray spectra, or from their spin-down when these NSs are seen as pulsars. While the former reflects a measure of the local surface field B_{surf} , the latter provides information on the global dipolar magnetic field B_d , if the spin-down is assumed to be solely due to dipolar electromagnetic emission. These two measures are not always in agreement, showing that the measured magnetic fields may have very different length-scales and intensities. In particular, they seem to suggest the presence of more intense and small-scale surface magnetic fields, together with less strong globally dipolar ones. For the pulsar 1E 1207.4-5209, for instance, the dipolar magnetic field estimated from the spin-down

rate is $B_d \sim 2 - 4 \times 10^{12}$ G (Pavlov et al. 2002), while the surface field estimated from the absorption features in its spectrum is $B_{\text{surf}} \sim 1.5 \times 10^{14}$ G (Sanwal et al. 2002). Similarly, observations of the pulsar RBS B1821-24 (Becker et al. 2003) indicate that $B_d \sim 10^9$ G, while $B_{\text{surf}} \sim 10^{11}$ G.

The existence of magnetic fields with different strengths and distributed on different length-scales can be explained in terms of a dynamo mechanism driven by the simultaneous presence of rotation and turbulent motions. During the first ~ 40 s after their birth, proto-neutron stars (PNSs) are expected to develop hydrodynamical instabilities (Epstein 1979; Livio et al. 1980; Burrows & Lattimer 1986), which can excite a hydro-magnetic dynamo. Such instabilities could be essentially of two types. The first one, driven by the entropy gradient, is a Rayleigh-type *convective instability* (CI) that operates in the inner regions of the star. The second one is a double diffusive instability, driven by both the entropy and leptonic gradients. This is usually referred to as the *neutron-finger instability* (NFI); it operates in the outer

PNS is assumed to be in hydrostatic equilibrium at all times), and no feedback from the magnetic field is taken into account in the conservation of momentum and energy. As a result, the velocity field is taken as pre-assigned and time-independent. This approximation works quite well as long as the magnetic field strength is small (i.e. as long as the magnetic pressure and tension are negligible in the Euler equations), but has the drawback that nothing prevents the indefinite growth of the magnetic field once a dynamo action is present. In real systems, the velocity profile will adjust itself in such a way as to reduce the efficiency of the dynamo and here, as a way of mimicking this feedback, we introduce two “*quenching functions*” (described later in more detail) that suppress the amplification as the total field increases above a certain threshold, thus leading the system towards saturation even in the absence of a consistent feedback.

Our model for the kinematic dynamo follows the one proposed by Rüdiger et al. (1994) and Blackman & Brandenburg (2002) and, in particular, we consider a velocity field

$$\mathbf{v} = (0, kx, 0) ,$$

and a magnetic field having components only in the (x, y) plane but with a vertical dependence

$$\mathbf{B} = (B_x(z), B_y(z), 0) .$$

The α -parameter and the magnetic diffusivity η are both expressed as the product of three terms

$$\alpha = \alpha_0 \alpha'(z, t) \psi_\alpha(\mathbf{B}) , \quad (2)$$

$$\eta = \eta_0 \eta'(z, t) \psi_\eta(\mathbf{B}) , \quad (3)$$

where α_0 and η_0 measure the strength of the α -effect and turbulent diffusion respectively, while $\alpha'(z, t)$ and $\eta'(z, t)$ represent the profiles of α and η in the two instability regions. More specifically, α' is chosen to be antisymmetric across the equatorial plane and different from zero only in the NFI zone, where the mean-field dynamo is at work. The turbulent diffusivity η' , on the other hand, is set to be of the order of unity in the NFI zone and about an order of magnitude larger in the turbulent CI zone. We implement these prescriptions by making use of the error function “erf” as

$$\alpha'(z, t) \equiv \begin{cases} \frac{1}{2} [1 + \text{erf}(-(z + \lambda)/d)] , & z \in [-H, 0] \\ -\frac{1}{2} [1 + \text{erf}((z - \lambda)/d)] , & z \in [0, H] \end{cases} \quad (4)$$

$$\eta'(z, t) \equiv \frac{1}{10} \left\{ 10 - \frac{9}{2} \left[1 + \text{erf}[(z - \lambda)/d] \right] \right\} \times \left\{ 10 - \frac{9}{2} \left[1 + \text{erf}[-(z + \lambda)/d] \right] \right\} , \quad (5)$$

where $\lambda \equiv z_1 + Vt$, with z_1 being the coordinate of the boundary between the CI and NFI zones and V the expansion velocity of the boundary layer. The quantity d represents the thickness of the interface between the CI and NFI zones and is used to obtain a smooth change of the error function, with smaller values leading to sharper changes; for the results reported here we have chosen $d/H = 0.04$. The profiles of α' and η' , as given by Eqs. (4) and (5), are shown in Fig. 2, with the solid and dashed lines indicating the initial conditions and the final conditions after 40 s, respectively.

Finally, $\psi_\alpha(\mathbf{B})$ and $\psi_\eta(\mathbf{B})$ appearing in Eqs. (2) and (3) represent the quenching functions for the α -effect and turbulent diffusion η , respectively. These terms are used to limit the otherwise unlimited growth of the magnetic field (α -quenching)

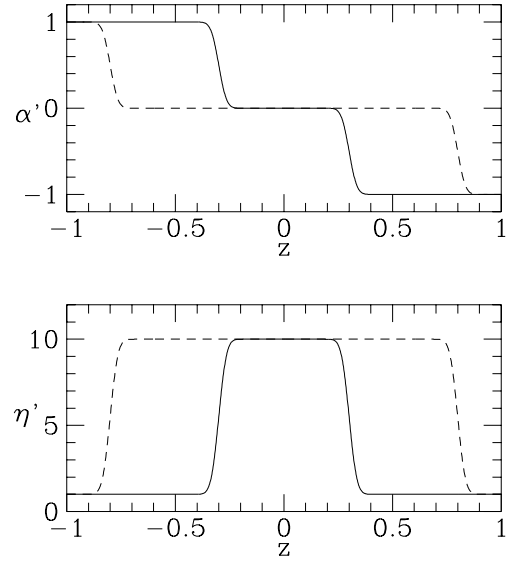


Fig. 2. Top panel: profiles of the normalized function α' at the beginning of the numerical simulation for $t = 0$ (solid line) and at the end of the numerical simulation for $t = 40$ s (dashed line); bottom panel: the same as in the top panel but for η' .

and suppress its turbulent diffusion (η -quenching). In general they are expected to have a different dependence on the magnetic field strength, but we here consider a single expression for the two functions in terms of the equipartition magnetic field $B_{\text{eq}} = \langle u \rangle \sqrt{4\pi\rho}$, where $\langle u \rangle$ is the mean velocity of turbulent eddies and ρ the mass-density

$$\psi_{\alpha, \eta}(\mathbf{B}) \equiv \left[1 + \int_{-H}^H \left(\frac{B}{B_{\text{eq}}} \right)^2 dz \right]^{-1} . \quad (6)$$

Making use of these definitions, Eq. (1) can be split into the following two coupled scalar partial differential equations

$$\partial_t B_x = -\partial_z(\alpha B_y) + \partial_z(\eta \partial_z B_x) , \quad (7)$$

$$\partial_t B_y = \partial_z(\alpha B_x) + B_x \partial_x v_y + \partial_z(\eta \partial_z B_y) , \quad (8)$$

which can also be written in a dimensionless form by scaling lengths in units of the semi-height of the cylinder H , times in units of the diffusion time $\tau_d = H^2/\eta_0$, and magnetic fields in units of B_{eq} . We also find it useful to introduce the dimensionless parameters

$$C_\alpha \equiv \alpha_0 \frac{H}{\eta_0} , \quad \text{and} \quad C_\Omega \equiv \partial_x v_y \left(\frac{H^2}{\eta_0} \right) = k \left(\frac{H^2}{\eta_0} \right) , \quad (9)$$

which represent the Reynolds numbers for the α -effect and the differential rotation, respectively. Furthermore, by introducing the standard vector potential $\mathbf{A} = [A_x(z), A_y(z), 0]$, so that the poloidal component of the magnetic field is $\mathcal{B}_p \equiv B_x = -\partial_z A_y$, we obtain the following dimensionless equations for the vector potential $\mathcal{A} = A_y$ and the toroidal component of the magnetic field $\mathcal{B}_t \equiv B_y$

$$\partial_t \mathcal{A} = C_\alpha \alpha(z, t) \psi_\alpha(B_{\text{tot}}) \mathcal{B}_t + \eta(z, t) \psi_\eta(B_{\text{tot}}) \partial_z^2 \mathcal{A} \quad (10)$$

$$\partial_t \mathcal{B}_t = -C_\alpha \partial_z [\alpha(z, t) \psi_\alpha (B_{tot}) \partial_z \mathcal{A}] - C_\Omega \partial_z \mathcal{A} + \partial_z [\eta(z, t) \psi_\eta (B_{tot}) \partial_z \mathcal{B}_t] \quad (11)$$

where $B_{tot} \equiv [\mathcal{B}_t^2 + (\partial_z \mathcal{A})^2]^{1/2}$. Once the initial conditions $\mathcal{B}_t(z, 0)$ and $\mathcal{A}(z, 0)$ are given, together with the parameters, C_α , C_Ω , α , η , ψ_α , ψ_η , and suitable boundary conditions at the stellar edges, it is possible to solve Eqs. (10) and (11) to describe the time evolution of the magnetic field. Our choice for the boundary conditions reflects the fact that we are interested in an adiabatic evolution of the magnetic field in the stellar interior, thus neglecting the energy losses related to a Poynting flux. Because of this, we simply set the magnetic fields at these locations to zero.

It is important to note that the parameters C_α and C_Ω are not linearly independent but can be related in terms of the strength of the differential rotation, of the pressure scale-height and of the “radius” of the PNS. To deduce this relation we recall that the $\alpha\Omega$ -dynamo assumes that $\alpha_0 \sim \Omega L_p$, where Ω is the angular velocity and L_p the pressure scale-height, so that

$$P \sim \frac{\xi}{C_\alpha} = \frac{2\pi L_p H}{C_\alpha \eta_0}, \quad (12)$$

where $\xi \equiv 2\pi L_p H / \eta_0$. For a typical PNS with mass $\sim 1 M_\odot$, $H \sim 15$ km and $L_p \sim 3$ km (Bonanno et al. 2003), $\eta_0 \sim L_p^2 / \tau_{\text{NFI}}$ ranges from $9 \times 10^{11} \text{ cm}^2 \text{ s}^{-1}$ for NFI eddy turnover times of 100 ms, up to $3 \times 10^{12} \text{ cm}^2 \text{ s}^{-1}$ for NFI eddy turnover times of 30 ms. Such values of η_0 yield typical diffusion timescales τ_p ranging from 0.75 s to 2.5 s, respectively. As a result, the parameter ξ is expected to be roughly in the range $1 \text{ s} \leq \xi \leq 3 \text{ s}$ for all of the relevant parameter space considered here.

In a similar way, since $\partial_x v_y = k \sim \Delta\Omega$, and defining the relative differential rotation strength as $q \equiv \Delta\Omega / \Omega \simeq (\Omega_s - \Omega_c) / \Omega_s$, where Ω_s and Ω_c are the angular velocities of the surface and the core respectively, it is possible to conclude that

$$q \sim \zeta \frac{C_\Omega}{C_\alpha}, \quad (13)$$

where $\zeta \equiv L_p / H \simeq 1/5$. Here we use $\Delta\Omega$ as a global measure of the rotational stress instead of using a necessarily arbitrary function that describes the behaviour of $\Omega(z)$ in the region between Ω_c and Ω_s . On the other hand we are severely limited by our ignorance of the detailed processes leading to the appearance of the differential rotation in the NFI zone of PNSs.

For all of the calculations reported here we assume that the angular velocity of the core is larger than that of the surface, so that $q < 0$ and, conservatively, we limit our analysis to values of $|q|$ not exceeding 10^2 , i.e. a core rotating 10^2 times faster than surface. Finally, by assuming a mass-density in the NFI zone $\rho \sim 10^{13} \text{ g cm}^{-3}$ and that the eddy convective velocities $\langle u \rangle \simeq L_p / \tau_{\text{NFI}} \sim 3 \times 10^6 \text{ cm s}^{-1}$, it follows that B_{eq} is of the order of 10^{13} G . The parameters defined in Eqs. (12) and (13) essentially determine the parameter space for the solutions of Eqs. (10) and (11).

3. Numerical method and tests

In order to solve the mixed parabolic-hyperbolic system of partial differential equations (10) and (11), we discretize the continuum space-time by replacing it with a two dimensional grid, where the two dimensions represent the space and the time variables, z and t , respectively. We use constant spacing in both directions, with a typical grid of 50 zones. Tests were performed with a larger number of gridpoints (100, 200 and 400) and have

revealed that a minimum of 50 gridpoints was sufficient to yield a small-enough truncation error. The evolution algorithm chosen is the FTCS (Forward-in-Time, Centered-in-Space) scheme, which gives a first-order approximation for the time derivatives and a second-order approximation for the space derivatives. Furthermore, stability requires the timestep to be $\Delta t = O(\Delta z^2)$ (we typically use $\Delta t = 10^{-2} \Delta z^2$), thus making the whole algorithm second-order both in space and in time. Using ghost-zones for implementing the boundary conditions, the final form of the finite-difference equations is

$$\mathcal{A}_j^{n+1} = \mathcal{A}_j^n + \Delta t d_j^n \mathcal{B}_j^n + k_1 a_j^n (\mathcal{A}_{j+1}^n - 2 \mathcal{A}_j^n + \mathcal{A}_{j-1}^n), \quad (14)$$

$$\begin{aligned} \mathcal{B}_j^{n+1} = & \mathcal{B}_j^n + k_2 c (\chi_{j+1}^n - \chi_{j-1}^n) + \\ & + k_2 b (\mathcal{A}_{j+1}^n - \mathcal{A}_{j-1}^n) + \\ & + k_1 a_j^n (\mathcal{B}_{j+1}^n - 2 \mathcal{B}_j^n + \mathcal{B}_{j-1}^n) + \\ & + k_2 f_j^n (\mathcal{B}_{j+1}^n - \mathcal{B}_{j-1}^n), \end{aligned} \quad (15)$$

where

$$\chi_j^n = e_j^n \frac{\mathcal{A}_{j+1}^n - \mathcal{A}_{j-1}^n}{2 \Delta z} \quad (16)$$

and

$$k_1 = \frac{\Delta t}{\Delta z^2}, \quad k_2 = \frac{\Delta t}{2 \Delta z} \quad (17)$$

$$a_j^n = \eta_j^n \psi_\eta^n, \quad b = -C_\Omega, \quad c = -C_\alpha \quad (18)$$

$$d_j^n = C_\alpha \alpha_j^n \psi_\alpha^n, \quad e_j^n = \alpha_i^n \psi_\alpha^n, \quad f_j^n = \frac{\eta_{j+1}^n - \eta_{j-1}^n}{2 \Delta z} \quad (19)$$

As a test of the code we have considered the equations when $C_\alpha = C_\Omega = 0$, $\psi_\eta = 1$ and $\eta(z, t) = 5 \cdot 10^{-2}$ so as to have two decoupled purely parabolic equations, and compared the numerical solution with the analytic one. The result of the comparison is that the maximum error is of the order of 2%.

We have also checked the convergence of the method by comparing the numerical solutions obtained with different spatial grids at a given time. The same continuum function $u(z, t)$ is approximated in a different way according to the space-time discretization: $u(z, t) = u_i^n(h) + \epsilon_h$, where ϵ_h is the truncation error. If we suppose that this error depends on the chosen space-interval h only, we can write: $\epsilon_h = k h^p$, with p being the order of convergence. It is then possible to deduce the following relation among the values of different discretized functions calculated at the same grid location i :

$$\frac{u_i^n(h) - u_i^n(h/2)}{u_i^n(h/2) - u_i^n(h/4)} = 2^p. \quad (20)$$

The value of p obtained as averaged over the spatial domain is 2.00 ± 0.01 , thus demonstrating a second-order convergence.

4. Analysis and results

While this analysis aims at a better understanding of the behaviour of the dynamos operating in the first stages of the life of a PNS, it is a long way from reproducing realistic conditions. This is partly due to the simplicity of the model employed, and partly to the still poorly constrained physical conditions of a newly born PNS. We recall that, according to Miralles et al.

Table 1. The parameters z'_1 (initial position of the boundary layer), V' (mean velocity of the boundary layer), and η -q (η -quenching activated or not) that define the configurations analyzed, and the ranges of values of B_s , C_α and $|q|$ used for the simulations. As regards C_α , we mainly used values between 5 and 200, since for smaller values the dynamo is not excited and for larger values the spin period would be too short.

	z'_1	V'	η -q	B_s/B_{eq}	C_α	$ q $
A	0.3	0.0	no	$10^{-7} - 10^{-1}$	$\leq 10^3$	$10^{-8} - 10^{-2}$
B	0.8	0.0	no	$10^{-7} - 10^{-1}$	$\leq 10^3$	$10^{-8} - 10^{-2}$
Aq	0.3	0.0	yes	$10^{-7} - 10^{-1}$	$\leq 10^3$	$10^{-8} - 10^{-2}$
Bq	0.8	0.0	yes	$10^{-7} - 10^{-1}$	$\leq 10^3$	$10^{-8} - 10^{-2}$
AB	0.3	0.0125	no	10^{-7}	$\leq 10^3$	$10^{-8} - 10^{-2}$
ABq	0.3	0.0125	yes	10^{-7}	$\leq 10^3$	$10^{-8} - 10^{-2}$

(2000, 2002), the NFI is expected to last only about 40 s, during which the NFI zone goes from occupying a large fraction of the envelope, to being confined to a small layer and then disappearing completely. We model this by assuming that the initial position of the NFI-CI boundary layer is at $z'_1 = 0.3H$ and the final one, after 40 s, is at $z'_1 = 0.8H$ (cf. Fig. 1), with an average expansion velocity of the layer that is $V = (z'_1 - z'_1)/t = 188 \text{ m s}^{-1}$ for $H = 15 \text{ km}$. In this case we also find it convenient to express all variables in terms of dimensionless quantities after introducing $z' \equiv z/H$, $t' \equiv t/\tau_D$, and $V' \equiv V\tau_D/H$. As a result, the coordinate position of the CI-NFI layer appearing in Eqs. (4) and (5) can be written as $\lambda = z'_1 + V't' = 0.3 + 0.0125 (\text{s}^{-1}) t (\text{s})$, where $-1 \leq z' \leq 1$, and $0 \leq t \leq 40 \text{ s}$, corresponding to a number of diffusion times ranging from 16 to 53, depending on the turnover time of the NFI eddies.

4.1. Initial models

As a representative sample of initial data we have considered six different models, four of which have the size of the NFI zone being constant in time, with either $z'_1 = 0.3$ (large instability zone) or $z'_1 = 0.8$ (small instability zone), and which are therefore referred to as *static*. For each of the two values of z'_1 we have examined the behaviour with and without η -quenching. Besides the static configurations, which are useful for studying the extreme cases of thick and thin NFI zones respectively, we have also considered two cases, which are referred to as *dynamical*, in which the NFI is allowed to shrink in time from the initial value of $z'_1 = 0.3$ to the final one of $z'_1 = 0.8$, over the 40 s during which the instability is expected to be active. For these dynamical models we have also studied the effect of activating or not activating the η -quenching. Such cases are useful for studying the role played by a dynamically shrinking NFI zone in the onset of the dynamo action and in the final magnetic fields obtained.

The static models are indicated as A, B, Aq, Bq, while the dynamical ones are indicated as AB and ABq; in all cases, the letter “q” is used to indicate whether or not η -quenching is taken into account. For all of these models we have carried out a large number of simulations by varying the seed magnetic field B_s , as well as the spin period P and the strength of the differential rotation $|q|$; all the models have been evolved for 40 diffusion times (i.e. between 30 s and 100 s). A summary of the properties of the different initial models and of the parameters used in the simulations is presented in Table 1.

4.2. Time evolution and critical period

The time evolutions of the average toroidal field \mathcal{B}_t and poloidal field \mathcal{B}_p (calculated in terms of their 2-norms) are shown in Figs. 3 and 4 respectively for the configuration Aq, with $|q| = 2$ and $C_\alpha = 4$ ($0.25 \text{ s} \leq P \leq 0.75 \text{ s}$), and for different values of the seed magnetic field B_s in the range $10^{-7} B_{\text{eq}} \leq B_s \leq 10^{-1} B_{\text{eq}}$.

For all of the configurations examined, the evolution of the magnetic field is rather similar and can be separated into two main stages: the first one is a transient phase during which the dynamo action amplifies the seed magnetic field exponentially; in the second phase the magnetic field instead reaches saturation around the equipartition value through the back reaction of the α -quenching. In general, the field reaches saturation within the 40 s lifetime of the NFI zone, except when the seed magnetic field is lower than $10^{-7} B_{\text{eq}}$ and $|q| \leq 2$. Nevertheless, in these cases the final magnetic value is of the order of $10^{-2} B_{\text{eq}}$, thus corresponding to 10^{11} G .

These two stages can easily be distinguished in Figs. 3 and 4, which report the time-evolution of the toroidal and poloidal magnetic fields, respectively. The secular slope of the curves in the exponential-amplification phase is clearly independent of B_s and constant in time, with $B = B_s e^{t/\tau_{\text{amp}}}$ and $\tau_{\text{amp}} \sim 0.6 \tau_D$, where $\tau_D \approx 25 \tau_{\text{NFI}}$ is the diffusion timescale. The growth-time however depends on $|q|$ and C_α , thus suggesting that the seed magnetic field determines only the time interval necessary to achieve the saturation, but not the final strength of the magnetic field. Clearly, if the initial field is too small, the dynamo cannot reach the saturation phase within 40 s. Other values of the growth times are $\tau_{\text{amp}} \sim 0.98 \tau_D$ for configuration ABq (with $C_\alpha = 4$ and $|q| = 3$) and $\tau_{\text{amp}} \sim 2.19 \tau_D$ for configuration B (with $C_\alpha = 29$ and $|q| = 4$).

It is possible that the combination of the rotation rate and differential rotation is not adequate to excite the dynamo and that the magnetic field is not amplified but rather decays with time. For each value of $|q|$ it is possible to find a threshold value of C_α such that for higher rotation rates (shorter periods) the dynamo is excited, while for lower rotation rates (longer periods) it is not. This value of C_α defines a *critical period* $\tilde{P}_c = P_c(|q|)$ through ξ [see Eq. (12)].

The presence of a critical period within the space of parameters is shown in Fig. 5 for the configuration A. The behaviour of the dynamo solutions is plotted as a function of the PNS spin period P and differential rotation strength $|q|$ for three different values of ξ (corresponding to different turnover times of the convective eddies in the NFI zone: $\xi = 1$, $\tau_{\text{NFI}} \approx 30 \text{ ms}$; $\xi = 2$, $\tau_{\text{NFI}} \approx 65 \text{ ms}$ and $\xi = 3$, $\tau_{\text{NFI}} \approx 100 \text{ ms}$). The three curves represent the thresholds between the regions in which the solutions of the dynamo equations grow in time (regions below the curves), thus allowing dynamo excitation, and the regions in which the solutions decay, thus preventing dynamo excitation. The three lines in Fig. 5 define therefore the critical dynamo period as a function of $|q|$, and it is evident that the critical spin velocity above which the dynamo operates decreases with increasing differential rotation. The behaviour of these curves suggests that it is possible to define a *global* critical period P_c as the minimum of \tilde{P}_c , so that if a PNS is rotating with a period shorter than P_c then for that PNS the dynamo will be excited.

The values of the global critical period obtained for the four static configurations are summarized in Table 2. Note that for a fixed value of ξ these periods depend only on the thickness of the NFI zone and are thus independent of the presence of η -quenching. As a result, in PNSs with larger NFI zones, the

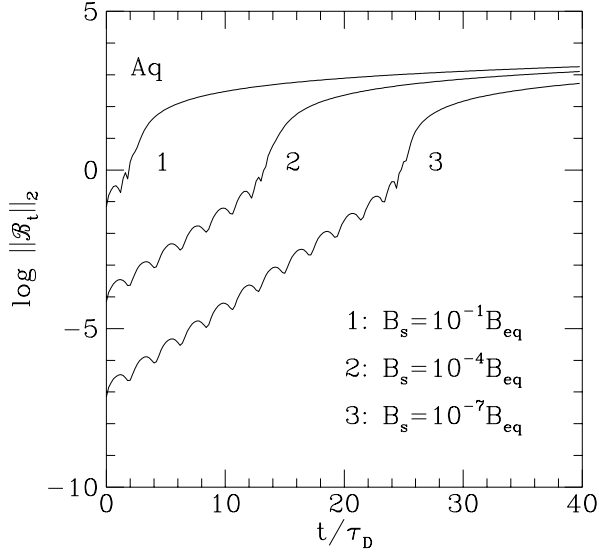


Fig. 3. Behaviour of the 2-norm of \mathcal{B}_t as a function of the number of diffusion times (t/τ_D) for the Aq configuration, $|q| = 2$, $C_\alpha = 4$ ($250 \text{ ms} \leq P \leq 750 \text{ ms}$), and for different seed magnetic field strengths, B_s . The growth-rate of the magnetic field during its amplification phase, before reaching the saturation, is almost independent of the seed magnetic field.

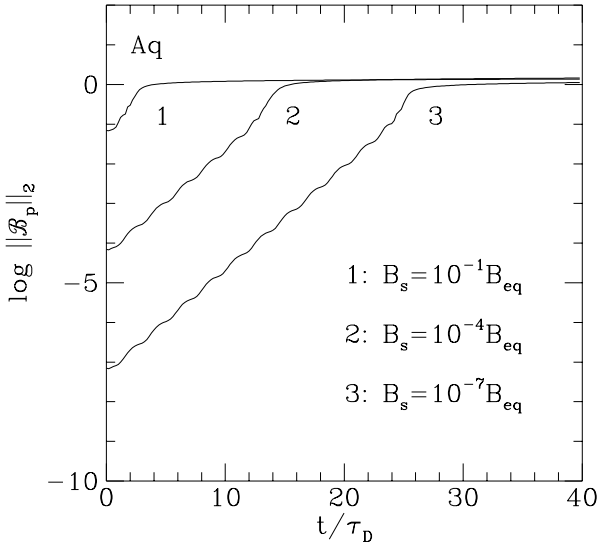


Fig. 4. The same as in the Fig. 3 but for \mathcal{B}_p .

dynamo action will be excited more easily, and thus at lower rotation rates, than for PNSs having smaller NFI zones.

Table 2. For each *static* configuration the critical value of C_α (C_α^C) and the corresponding global critical period of the PNS, $P_c = \xi/C_\alpha^C$ ms, for $\xi \in [1, 3]$ are reported.

	C_α^C	P_c [ms]
A	5	200 – 600
B	30	33 – 99
Aq	5	200 – 600
Bq	30	33 – 99

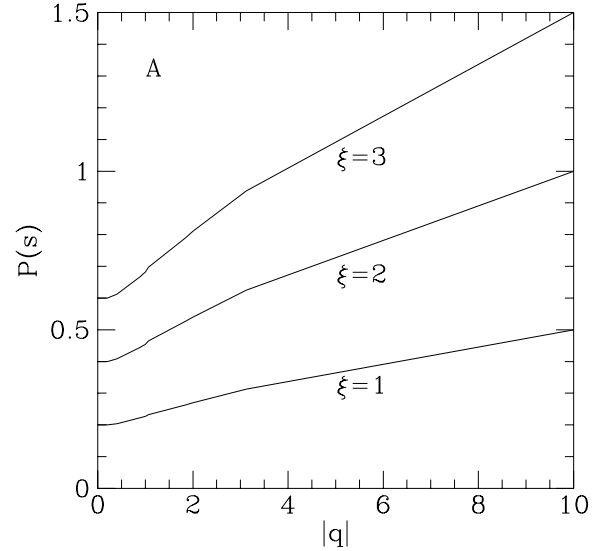


Fig. 5. Behaviour of the dynamo solutions as a function of the PNS spin period P and of the differential rotation strength $|q|$ for three different values of ξ , related to the turnover time of the convective eddies in the NFI zone.

4.3. The role of thickness of the NFI zone

Since the NFI zone is the region where the mean field dynamo is at work, it is natural to expect that by increasing the size of this part of the star the efficiency of the dynamo will also increase. To quantify this “improved efficiency” we can compare the results obtained for two configurations: one in which the NFI zone occupies 70% of the star (configuration A) and another one in which it covers 20% (configuration B). Reducing the extent of the active part of the star has two main effects: reducing the critical period and reducing the intensity of the final magnetic field.

The first of these effects has already been discussed in the previous section, and from Table 2 it is possible to note that reducing the NFI zone by a factor of 3.5 decreases the critical period by a factor of 6. To quantify the second effect we consider the ratio between the final strength of the magnetic field in configurations A and B, as a function of the differential rotation parameter $|q|$ and of C_α . As expected, the toroidal magnetic field for the configuration A is larger than the one for configuration B, regardless of any other parameter. The value of the ratio is reported in Table 3 and it should be noted that it is really only the toroidal-field ratio that changes with C_α , with the poloidal-field

Table 3. Ratio of the final intensity of the magnetic field in configurations A and B. The values in the table are calculated for $|q| > 10$. For $|q| < 10$ we still have $\mathcal{B}_t^{\text{fin}}(A)/\mathcal{B}_t^{\text{fin}}(B) > 1$ and $\mathcal{B}_p^{\text{fin}}(A)/\mathcal{B}_p^{\text{fin}}(B) < 1$, but the exact value depends on the differential rotation.

	C_α		
	50	100	200
$\mathcal{B}_t^{\text{fin}}(A)/\mathcal{B}_t^{\text{fin}}(B)$	13.4	6.6	13.0
$\mathcal{B}_p^{\text{fin}}(A)/\mathcal{B}_p^{\text{fin}}(B)$	0.38	0.37	0.37

ratio being essentially independent of the differential rotation or the spin period.

4.4. Asymptotic states of the static configurations

The value of the magnetic field after 40 s of evolution for some representative cases of the static configurations is shown in Figs. 6–9, which report the final intensity of the toroidal and poloidal components as functions of $|q|$ and for different values of C_α .

Figures 6 and 7 refer to configurations without η -quenching and show that the qualitative evolution of the field is independent of the rotation rate of the star. Furthermore, for small values of the differential rotation, i.e., for $|q| \lesssim |q^*|$, where $|q^*|$ is a representative threshold value, both the toroidal \mathcal{B}_t and poloidal \mathcal{B}_p components of the magnetic field are constant with $|q|$, while for $|q| \gtrsim |q^*|$, \mathcal{B}_t begins to increase and \mathcal{B}_p to decrease, following power-laws with exponents of the same magnitude but opposite signs (see Table 4). Note that the value of $|q^*|$ is smaller for high spin rates since the dynamo is more easily excited when the star is rapidly rotating.

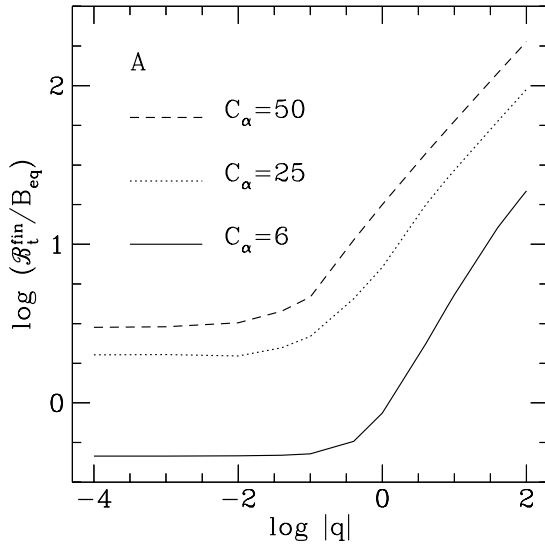


Fig. 6. Intensity of the final toroidal field \mathcal{B}_t , in units of B_{eq} , at the end of the 40 s NFI evolution time, as a function of the differential rotation parameter $|q|$ for different values of C_α . The simulation refers to the configuration A, thus without η -quenching.

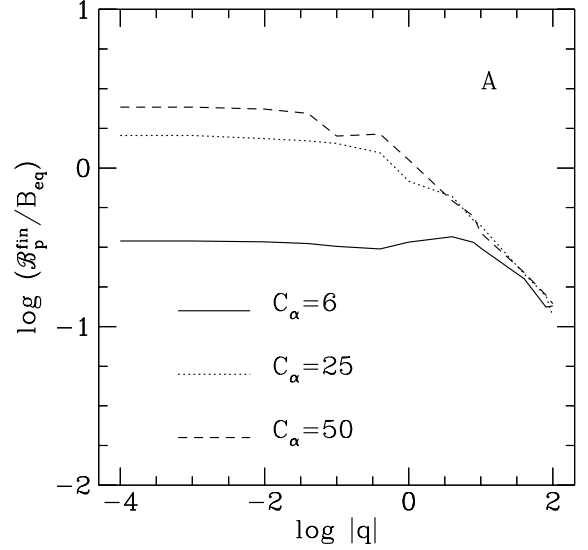


Fig. 7. The same as in Fig. 6 but for \mathcal{B}_p .

Figures 8–9, on the other hand, show the influence of η -quenching on the mean-field dynamo by comparing the final intensities of the magnetic fields for configurations for which the quenching is either active or not, i.e., configurations Aq and A, respectively. It is quite evident that the main consequence of η -quenching is to increase the amplification factor of the dynamo by several orders of magnitude, leaving the qualitative behaviour of the magnetic field unchanged, except for a value of $|q^*|$ significantly smaller.

A way of interpreting these results is to recall that the inclusion of η -quenching enhances the transformation of the poloidal magnetic field into a toroidal one (i.e., Ω -effect) and therefore enhances the importance of differential rotation. In addition, by reducing the magnetic diffusion, η -quenching effectively favors the amplification of the magnetic field (which becomes essentially frozen with the fluid), increasing the exponential growth-rate of the intensity; in the case shown in Fig. 11 it goes from $\tau_{\text{amp}} \sim 0.6 \tau_D$ to $\tau_{\text{amp}} \sim 0.8 \tau_D$. After a few diffusion times the α -quenching stops the amplification, leading the system towards saturation.

A typical example of the spatial distribution behaviour of the magnetic field is reported in Fig. 10, where we show the behaviour of the toroidal field strength, in terms of B_{eq} , as a function of the z coordinate at different time steps for the configuration Aq. As expected, the field is mainly localized in the NFI regions where $\alpha \neq 0$.

A couple of remarks are worth making at this point. Firstly, while the figures in this section refer only to the configurations A and Aq, the same behaviour has also been found for the configurations B and Bq, thus indicating that the results presented here are independent of the extent of the NFI zone. Secondly, the extreme magnetic-field amplifications obtained are a direct consequence of the idealized setup used in our modeling of the PNS. We expect that a more realistic description of the geometry of the star and a consistent treatment of the feedback of the magnetic field on the dynamics of the plasma will lower these

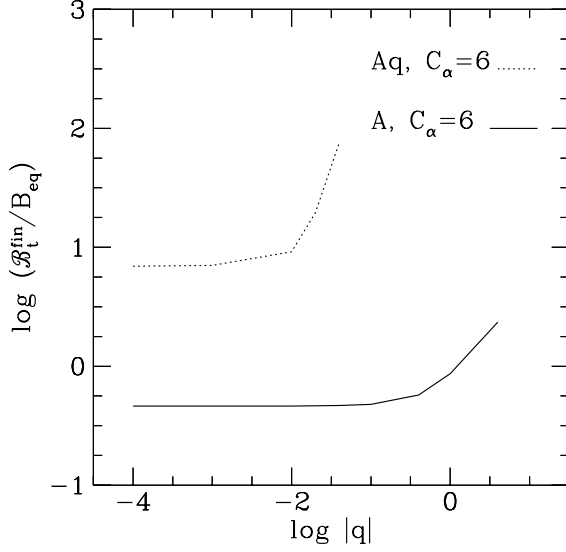


Fig. 8. Intensity of the toroidal field \mathcal{B}_t in units of B_{eq} , at the end of the 40 s NFI evolution time, plotted as a function of the differential rotation parameter $|q|$ for $C_\alpha = 6$ ($167 \text{ ms} < P < 500 \text{ ms}$), and an initial seed magnetic field of $10^{-7} B_{\text{eq}}$. The simulation shows the comparison between a configuration with η -quenching (Aq) and without η -quenching (A).

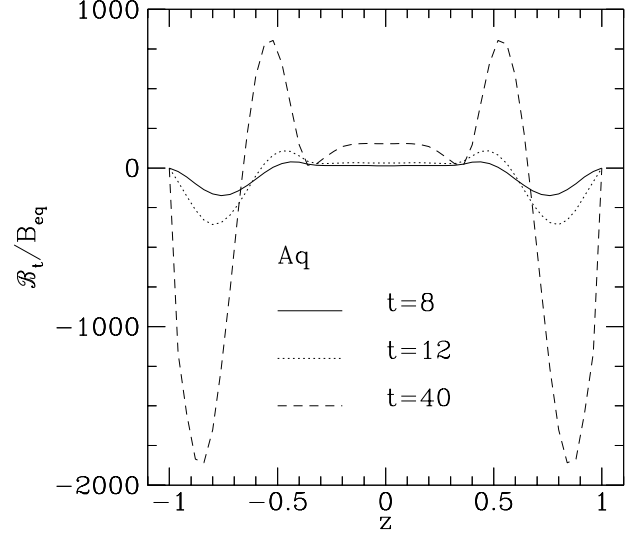


Fig. 10. Spatial distribution of the toroidal component of the magnetic field at different time steps, for configuration Aq, with $C_\alpha = 10$ and $|q| = 0.1$. For this configuration α is different from zero only in regions with $|z| > 0.3$.

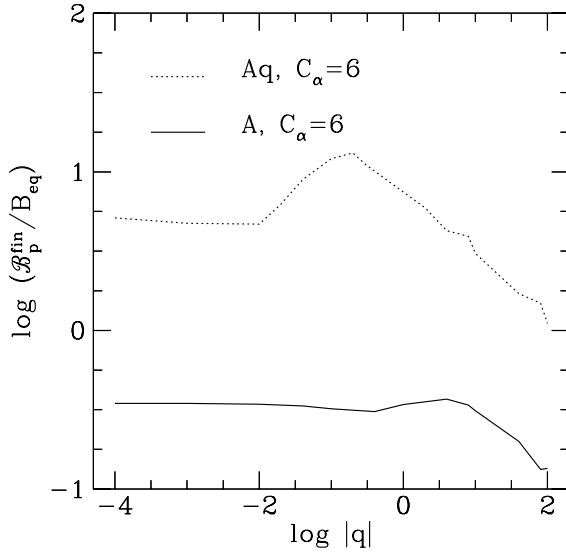


Fig. 9. The same as in the Fig. 8 but for \mathcal{B}_p .

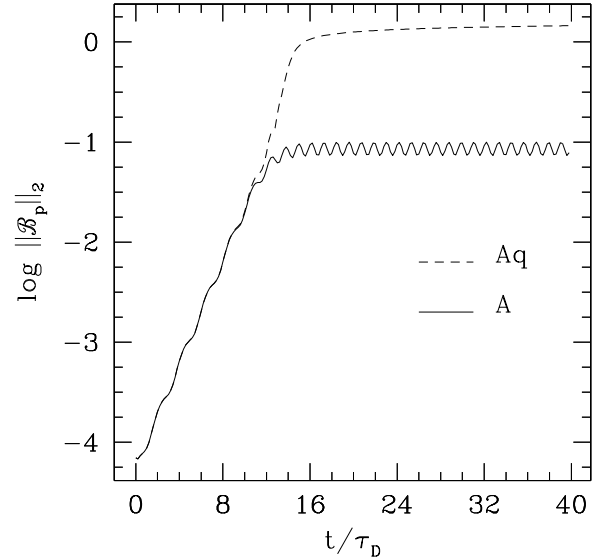


Fig. 11. Behaviour of the 2-norm of \mathcal{B}_p as a function of the number of diffusion times (t/τ) for the A and Aq configurations, $|q| = 2$, $C_\alpha = 4$ ($250 \text{ ms} \leq P \leq 750 \text{ ms}$), and for seed magnetic field strengths of $B_s = 10^{-4} B_{\text{eq}}$. The growth-rate of the magnetic field during its first amplification phase is the same for both configurations, which are eventually driven to saturation by the α -quenching.

estimates, yielding magnetic fields which are less strong but still comparable or larger than the equipartition value.

4.5. Asymptotic states of the dynamical configurations

Although equally idealized, the two *dynamical* configurations AB and ABq are expected to provide a better modeling of the first 40 s of life of the PNS, during which the thickness of the NFI region is assumed to vary from about 70% of the PNS radius, down to about 20% of it (*cf.* the profiles of α and η in Fig. 2). However, besides the fact that for these configurations it is not possible to define a unique critical period, since it depends on the NFI zone thickness (*cf.* Sect. 4.2), we have found that the qualitative behaviour of the magnetic field for dynamical configurations is very similar to that discussed in the previous section for the static configurations.

More specifically the most salient difference is that, because of the shrinking of the instability zone, the overall amplification is reduced with respect to the A configurations and increased with respect to the B configurations. Indeed, at the beginning of the evolution the NFI zone is as large as that of the A configurations, and at the end it is as large as that of the B configurations. Nevertheless, if one considers a spin rate and a differential rotation strength high enough to have the dynamo mechanism active during all the instability period (*i.e.* C_α and $|q|$ larger than the critical values of the B configurations), then the final field is comparable to or even larger than, that in the static A configurations.

4.6. The effect of Lorentz force backreaction on differential rotation

Several authors (*e.g.*, Weiss et al. 1984; Belvedere et al. 1990; Roald & Thomas 1997; Moss & Brooke 2000; Gilman & Rempel 2005; Covas et al. 2005; Rempel 2006) investigated the effect of the backreaction generated by the Lorentz-force on plasma motion; this is sometimes referred to as the “Malkus-Proctor effect”. These investigations indicate that the dynamo-intensified toroidal field interacts, via the Lorentz force, with the zonal flow (predominantly azimuthal), thus limiting the growth of differential rotation and reducing its strength. An obvious consequence of this effect is that the amplification of the toroidal field itself is also diminished. All of the above mentioned studies, which were mainly devoted to the analysis of the Sun or solar-type stars, made use of an additional Euler equation in order to include the Lorentz force consistently.

This is different from what is done in our simple, idealized model case, where we use the induction equation only, and assume the rotational stress $\Delta\Omega$ to remain constant in time for each configuration. As a result, any phenomenological, parameterized effect of the magnetic field on the already fixed $\Delta\Omega$ would not be consistent with our basic assumptions.

Nevertheless we performed some runs with a phenomenological quenching function applied to C_Ω (Ω -quenching), of the same type as those applied to α and η . The result of these runs shows a moderate reduction of the final strength of the toroidal field for all the examined cases. This result, however, might be somewhat misleading. Our dynamo is essentially an $\alpha^2\Omega$ one, which can shift to an $\alpha\Omega$ dynamo at strong rotational stresses, with dynamo numbers (see Sect. 4.7) given by the products $C_\alpha^2 C_\Omega$ and $C_\alpha C_\Omega$ respectively. Therefore, the use of an Ω -quenching applied to C_Ω essentially amounts to applying a stronger quenching to α (and this explains the reduction of the toroidal field strength), but does not limit the fixed rotational stress.

A rough estimate of the importance of magnetic field backreaction on differential rotation can be made in terms of the

“Elsasser” number $\Lambda = B^2/8\pi\rho\Omega\nu$ (Rüdiger & Hollerbach 2004), namely the ratio of magnetic to zonal flow energy. If $\Lambda \ll 1$ the backreaction effect is negligible, while for $\Lambda \gg 1$ it is of overwhelming importance, and should produce a strong reduction of differential rotation. If we define an equipartition $\Lambda_{\text{eq}} = B_{\text{eq}}^2/8\pi\rho\Omega\eta_0$ and assume that the turbulent viscosity ν is of the same order of turbulent magnetic diffusion (*i.e.*, both momentum and magnetic field are transported by the same eddies), we have $\Lambda = h^2\Lambda_{\text{eq}}$, where $h = B_t/B_{\text{eq}}$. For the typical values of our PNSs given in Sect. 2, $\Lambda \simeq 0.05$ at equipartition, while for magnetic field strengths exceeding the equipartition value by two or three orders of magnitude, the effect of the Lorentz force on differential rotation cannot be neglected.

Our simplified model does not allow us to predict the intensity of this effect, even though we obviously expect that the final magnetic field will be comparable to or slightly larger than the equipartition one. It is also worth pointing out that a reduction or suppression of differential rotation does not necessarily imply a suppression of the dynamo, since the $\alpha^2\Omega$ can shift to a pure α^2 dynamo. Furthermore we cannot either predict whether the strong toroidal fields generated are stable against the magneto-rotational or Tayler instabilities, which would require a dynamical analysis, beyond the scope of the present exploratory study; this will be addressed in a more realistic model we intend to develop in the future.

4.7. A general expression for the final magnetic field

From the discussion about the time evolution of the solutions of Eqs. (10) and (11) (*cf.* Sect. 4.2) and about their asymptotic states (*cf.* Sect. 4.4 and 4.5), it is apparent that the configurations considered in this work have common features that we believe reflect a fundamental behaviour of the mean field dynamo process. Thus we expect these features to be present also when the toy model considered here is replaced by a more realistic one. In what follows we discuss how to summarize these analogies by presenting a general expression for the final magnetic field.

Using Figs. 6 and 7 as guides, it is easy to recognize the existence of a transition value $|q^*|$ such that for $|q| \lesssim |q^*|$ the final magnetic field does not depend on the degree of differential rotation, while for $|q| \gtrsim |q^*|$ it increases as a power-law. We therefore express this increase with a phenomenological relation of the type

$$\mathcal{B}_t^{\text{fin}} = K_t (C_\alpha)^{\delta_t} |q|^{\gamma_t}, \quad (21)$$

$$\mathcal{B}_p^{\text{fin}} = K_p (C_\alpha)^{\delta_p} |q|^{\gamma_p}, \quad (22)$$

where the indices t and p refer to the toroidal and poloidal components, respectively. Note that the threshold value $|q^*|$ may well differ between (21) and (22), and that the constants $K_{t,p}$ depend on the particular configuration, *i.e.* on the profile of α and η and on η -quenching.

Using a power-law fit, we have calculated the values for the exponents in the phenomenological expressions (21) and (22) and collected them in Table 4 for both the static and the dynamical models, with and without η -quenching. The reported values of $\gamma_{t,p}$ have been computed using several configurations having different C_α (between 6 and 200), while those for $\delta_{t,p}$ have been derived from configurations differing by the amount of differential rotation ($|q|$ in the range $10^{-1} - 10^2$). For all of the configurations considered, the variance around the reported values is very small and of a few percent only.

Overall, the data in Table 4 show that both γ_t and γ_p are very close to either 1/2 or -1/2 (with the exception of Aq, for

Table 4. Indices of the power-law behaviour found in the dependence of B^{fin} on the degree of differential rotation $|q|$ and the spin rate C_α . The errors, not reported in the table, are of a few percent only.

	γ_t	γ_p	δ_t	δ_p
A	0.53	-0.48	1.00	0.03
B	0.51	-0.49	1.00	0.00
AB	0.49	-0.48	0.94	0.09
Aq	0.77	-0.37	1.10	0.06
Bq	0.54	-0.48	1.09	0.07
ABq	0.56	-0.46	1.13	0.12

which they are ~ 0.75 and ~ -0.35 , respectively) and that quite generically $|\gamma_t| + |\gamma_p| \approx 1$. We can therefore rewrite expressions (21)–(22) simply as

$$\mathcal{B}_t^{\text{fin}} \simeq K_t C_\alpha |q|^{1/2}, \quad (23)$$

$$\mathcal{B}_p^{\text{fin}} \simeq K_p |q|^{-1/2}. \quad (24)$$

The behaviour of the toroidal and poloidal final fields in the super-critical dynamo regime, as given by Eqs. (23) and (24), can be understood in terms of the characteristic dynamo parameters, C_α and C_Ω . The first parameter represents the dynamo’s ability to regenerate the poloidal field from the toroidal one (i.e., α -effect), while the second parameter the dynamo’s ability to regenerate the toroidal magnetic field from its parent poloidal field, via the action of differential rotation (i.e., Ω -effect). Both parameters are important as they define the “*dynamo number*”, given by $N_{\alpha\Omega} \equiv C_\alpha C_\Omega$ for an $\alpha\Omega$ dynamo, and $N_{\alpha^2\Omega} = C_\alpha^2 C_\Omega$ for an $\alpha^2\Omega$ dynamo. In essence, below a certain critical number N_c , which depends on the specific model considered, no dynamo action is possible, while the dynamo becomes ever more efficient as N increases.

In our case, when the effect of differential rotation becomes important (i.e., high $|q|$ values), our dynamo behaves essentially as an $\alpha\Omega$ dynamo with $C_\Omega/C_\alpha \approx 5|q| \gg 1$ [see Eq. (13)]. For this dynamo, the ratio of the toroidal to the poloidal field, $\mathcal{B}_t/\mathcal{B}_p \approx (C_\Omega/C_\alpha)^{1/2}$, is high, as verified also with our nonlinear calculations (see Figs. 6 and 7), with typical values ranging from 20 to 30. The relationships described by Eqs. (23) and (24) have been derived in the super-critical regime region where \mathcal{B}_t substantially increases and \mathcal{B}_p decreases with increasing C_Ω or $|q|$ for each fixed C_α value (see Figs. 6 and 7 for $\log|q| > 0$). Therefore, it is not surprising that $\mathcal{B}_t \propto N^{1/2}$ [Eq. (23)], namely that the toroidal field increases with dynamo efficiency. On the other hand, the poloidal field $\mathcal{B}_p \propto C_\alpha/N^{1/2}$ [Eq. (24)] will necessarily decrease with dynamo efficiency increase, since the increase of N is only due to the increase of C_Ω (C_α is kept fixed for each simulation). This is consistent with the fact that, at high differential rotation rates, the zonal flow dominates with respect to the vertical motions (predominantly radial) thus reducing the strength of convection and therefore the efficiency of the α -effect, namely the regeneration of the poloidal field.

We expect that more sophisticated calculations will produce changes of these values reported in Eqs. (23) and (24), especially in the transition between the $\alpha^2\Omega$ and the $\alpha\Omega$ dynamos, and when the Lorentz-force feedback is properly taken into account. However, we expect that the behaviour of the magnetic field as given by Eqs. (23) and (24) will remain unaltered.

5. Conclusions

We have presented a toy model to describe the amplification of the magnetic field inside a proto-neutron star (PNS) via a dynamo action. The model assumes that a neutron-finger instability (NFI) develops in the outer regions of a PNS during the early stages of its life as discussed by Miralles et al. (2000, 2002), and that the conditions for the generation of a mean-field dynamo process are met. Although highly simplified by being only one-dimensional and by adopting the kinematic approximation, our model aims to capture the qualitative features of the dynamo action by including a moving boundary of the instability zone and the nonlinearities introduced by the feedback processes, which saturate the growth of the magnetic field (i.e. α -quenching) and suppress its turbulent diffusion (i.e. η -quenching).

In essence, the amplification of the magnetic field is described in terms of a system of coupled partial differential equations of mixed hyperbolic-parabolic type, which are solved numerically for a very large variety of initial conditions. These include varying the spin period of the PNS, the strength of the differential rotation between the core and the surface, the intensity of the primordial (seed) magnetic field, and the extent of the NFI zone.

Overall, we have found that, independently of whether the size of the NFI zone varies in time or not, the amplification of the magnetic field undergoes a first exponential increase with growth-time that is the same for both the toroidal and the poloidal components of the magnetic field. The exact value of the growth-time depends on several parameters and it is roughly in the range $\tau_{\text{amp}} \sim [0.5 - 2.5] \tau_D$, with τ_D being the diffusion timescale. The exponential growth then stops through the back reaction of the α -quenching and the magnetic field reaches saturation. The final magnetic field produced at the end of the 40 s of evolution does not depend sensitively on the initial magnetic field, but it does depend on whether the η -quenching is active or not, becoming 2-3 orders of magnitude larger in the first case.

Despite its crudeness, our model is also able to capture another important feature of the dynamo mechanism, namely the existence of a critical rotation period P_c , above which no dynamo action is possible and the magnetic field simply decays (Bonanno et al. 2003). For periods near the critical one, on the other hand, the dynamo is just able to sustain the magnetic field close to its initial value, thus avoiding its decay. However, as the spin rate (or the degree of differential rotation) is increased, the dynamo becomes more and more efficient, amplifying the magnetic field up to values several orders of magnitude larger than the equipartition magnetic field. These very high intensities ($10^{18} G$ for the toroidal component and $10^{14} G$ for the poloidal one) may seem unphysical at first sight; however, here we are considering magnetic fields still inside the neutron star and only the poloidal component is thought to emerge afterwards. Determining the critical period accurately is important to constrain the fraction of neutron stars that may undergo this magnetic-field amplification at birth, and we have found that P_c is in the range 33 – 600 ms for rigidly rotating PNSs, becoming larger as the degree of differential rotation is increased. As a result, as long as we have no general constraints on the strength of the differential rotation, a lower limit of $P \approx 30$ ms can be taken as the generic threshold below which a mean-field dynamo may be active in a newly born PNS.

Another interesting result of this investigation is that, despite the large parameter space considered, the final value of the magnetic field seems to follow a surprisingly robust dependence with the spin period and the degree of differential rotation, both of

which can be summarized in a phenomenological expression of the type

$$\mathcal{B}^{fin} \propto (C_a)^\delta |q|^\gamma \quad (25)$$

which holds only for $|q|$ larger than a transition level of differential rotation $|q^*|$, whose exact value depends on the configuration and on the other parameters (overall it is in the range $10^{-2} - 10^1$). The exponents δ , γ are different for the toroidal and poloidal magnetic field components and depend only very weakly on all of the parameters varied in this analysis. In particular, for the toroidal magnetic-field component we have found $\delta \sim 1$ and $\gamma \sim 1/2$, while for the poloidal one $\delta \sim 0$ and $\gamma \sim -1/2$. The exact values of these exponents are likely to be modified by more realistic and multidimensional calculations, but we also expect that the scaling in expression (25) will persist in further refinements of this treatment.

The work presented here can be improved in a number of different ways. A first possibility is a more realistic description of the geometry of the problem, with a two or three-dimensional description of the PNS. A second and computationally less expensive alternative is that of improving the nonlinear feedback of the magnetic field on the dynamics of the matter. This can be done by using the same geometry adopted here, but coupling the mean-field induction equation (1) with the solution of the MHD equations for the conservation of energy and momentum.

Acknowledgements. We are grateful to V. Urpin and J. C. Miller for their useful comments and suggestions. This work was partially supported by the Italian Ministry of University and Research under the contract PRIN 2004024993.

References

- Becker, W., Swartz, D., Pavlov, W. et al. 2003, ApJ 594, 798
 Belvedere, G., Piatella, R. M., & Proctor, M. R.E. 1990, GAFD 51, 263
 Blackman, E. G., & Brandenburg, A. 2002, ApJ 579, 359
 Bonanno, A., Rezzolla, L., & Urpin, V. 2003, A&A 410, L33
 Bonanno, A., Urpin, V., & Belvedere, G. 2005, A&A 440, 199
 Bonanno, A., Urpin, V., & Belvedere, G. 2006, A&A 451, 1049
 Brandenburg, A., Krause, F., Meinel, R., Moss, D., & Tuominen, I. 1989, A&A 213, 411
 Bruenn, S. W., Raley, E. A., & Mezzacappa, A. 2007, astro-ph/0404099
 Buras, R., Janka, H.-Th., Rampp, M., & Kifonidis, K. 2006, A&A 457, 281
 Burrows, A., & Lattimer, J. 1986, ApJ 307, 178
 Covas, E., Moss, D., & Tavakol, R. 2005, A&A 429, 657
 Dessart, L., Burrows, A., Livne, E., & Ott, C. D. 2006, ApJ 645, 534
 Epstein, R. 1979, MNRAS 188, 305
 Gilman, P. A., & Rempel, M. 2005, ApJ 630, 615
 Livio, M., Buchler, J., & Colgate, S. 1980, ApJ 238, L139
 Mezzacappa, A., Calder, A.C., Bruenn, S.W., Blondin, J.M., Guidry, M.W., Strayer, M.R. & Umar, A.S. 1998, ApJ 495, 911
 Miralles, J., Pons, J., & Urpin, V. 2000, ApJ 543, 1001
 Miralles, J., Pons, J., & Urpin, V. 2002, ApJ 574, 356
 Moss, D., & Brooke, J. 2000, MNRAS 315, 521
 Pavlov, G., Zavlin, V., Sanwal, D., & Truemper, J. 2002, ApJ 569, L95
 Rempel, M. 2006, ApJ 647, 675
 Roald, C. B., & Thomas, J. H. 1997, MNRAS 288, 551
 Rüdiger, G., & Arlt, R. 1996, A&A 316, L17
 Rüdiger, G., & Hollerbach, R. 2004, The Magnetic Universe: Geophysical and Astrophysical Dynamo (Wiley)
 Rüdiger, G., Kitchatinov, L. L., Küker, M., & Schultz, M. 1994, GAFD 78, 247
 Sanwal, D., Pavlov, G., Zavlin, V., & Teter, M. 2002, ApJ 574, L61
 Thompson, C., & Duncan, R. 1993, ApJ 408, 194
 Weiss, N. O., Cattaneo, F., & Jones, C. A. 1984, GAFD 30, 305
 Xu, R. X., & Busse, F. H. 2001, A&A 371, 963